Environmental Science Nano

ROYAL SOCIETY OF CHEMISTRY

PAPER

View Article Online
View Journal | View Issue





Cite this: *Environ. Sci.: Nano*, 2020, 7, 1126

# Enhanced uptake of glyoxal at the acidic nanoparticle interface: implications for secondary organic aerosol formation†

Qiuju Shi,‡[a] Weina Zhang,‡[a] Yuemeng Ji, *[a] Jiaxin Wang,[a] Dandan Qin,[a] Jiangyao Chen, [ab] Yanpeng Gao,[a] Guiying Li [ab] and Taicheng An [a]

Received 6th January 2020,
Accepted 27th February 2020

DOI: 10.1039/d0en00016g

rsc.li/es-nano

Glyoxal (GL) represents an important precursor of a secondary organic aerosol (SOA) and has broad biogenic and anthropogenic sources, but the interfacial chemistry of GL contributing to SOA formation is uncertain. Here, we performed molecular dynamics (MD) simulations and quantum chemical (QC) calculations to examine the interfacial process of gaseous GL on aqueous nanoparticles, including probing the GL attraction to the nanoparticles, uptake at the air–nanoparticle interface, and the hydration reaction within the nanoparticles under neutral and acidic conditions. The MD simulations show that the carbonyl O-atom of GL exhibits a preferential orientation to the air–nanoparticle interface. The acidic nanoparticle interface displays a preference for the uptake of gaseous GL relative to the neutral nanoparticle interface, showing that the presence of sulfuric acid (SA) enhances the adsorption and accommodation for GL. In addition, SA accelerates the aqueous reaction of GL inside the interior region of the nanoparticle, which indirectly promotes the uptake at the nanoparticle interface. Our results reveal the significantly enhanced uptake of GL at the acidic nanoparticle interface, highlighting the necessity to account for the interfacial process when assessing SOA formation.

### Environmental significance

Despite the role as the dominant constituent in fine particulate matter, the chemical mechanisms for secondary organic aerosol (SOA) formation remain poorly understood. Small α-dicarbonyls of glyoxal and methylglyoxal are produced in large quantities (about 185 Tg $y^{-1}$) from biogenic and anthropogenic emissions. Previous experimental studies have shown puzzling results concerning their contributions to SOA growth. Our work investigates the mechanism of gaseous GL approaching and entering the nanoparticles, including the attraction to the nanoparticles, uptake at the air–nanoparticle interface, and the hydration reaction within the nanoparticle, as well as its role in SOA formation. Our combined molecular dynamics and quantum chemical results provide insight into the importance of the interface in the atmospheric chemistry of GL towards SOA formation. Our results reveal the significantly enhanced uptake of GL at the acidic nanoparticle interface, highlighting the necessity to account for the interfacial process when assessing SOA formation.

## 1. Introduction

A secondary organic aerosol (SOA), a major component of the global fine particulate matter (PM2.5), profoundly impacts the Earth's atmospheric system in several aspects, such as visibility, cloud formation, climate and human health.[1–3] In the troposphere, SOA originates from the photochemical oxidation of volatile organic compounds (VOCs); this process yields various products that engage in the subsequent gas-to-particle conversion.[1,4] Glyoxal (GL) is an important product of the photochemical oxidation of biogenic (isoprene) and anthropogenic (aromatics) VOCs[5–7] with a global source of 45 Tg $yr^{-1}$.[8] Hence, GL is estimated to contribute a global SOA source of 2.6 Tg C $a^{-1}$.[8]

Growing evidence also reveals that GL exposed to ammonium sulfate and amine-containing seed nanoparticles can significantly contribute to brown carbon (BrC) formation.[9–12] For example, a previous experimental study identified that N-heterocycles, as the major component of BrC, could be formed from the aqueous reactions of GL and methylglyoxal with amines using orbitrap-mass spectrometry and thermal desorption-ion drift-chemical ionization mass spectrometry.[9] Other experimental studies have indicated that GL undergoes a polymerization reaction to produce low-

[a] *Guangdong Key Laboratory of Environmental Catalysis and Health Risk Control, Guangzhou Key Laboratory Environmental Catalysis and Pollution Control, School of Environmental Science and Engineering, Institute of Environmental Health and Pollution Control, Guangdong University of Technology, Guangzhou 510006, China. E-mail: jiym@gdut.edu.cn*
[b] *Synergy Innovation Institute of GDUT, Shantou 515041, China*

† Electronic supplementary information (ESI) available. See DOI: 10.1039/d0en00016g

‡ Both authors contributed equally to this work.

volatility oligomers in the aqueous phase.[13–17] Also, the heterogeneous reaction of GL catalyzed by sulfuric acid (SA) has been suggested to promote the formation of SOA.[13,18–20] However, the atmospheric mechanism of GL for the formation of SOA still remains unclear due to the lack of detailed information about the physicochemical behavior of GL in multiphase chemistry.[2]

Multiphase chemistry in aqueous nanoparticles is governed by the interfacial process as well as liquid-phase diffusion and reactions, that is, two main reaction regions are involved: the air–nanoparticle interface[21] and the nanoparticle interior.[14] The nanoparticle interface especially plays a crucial role[22] because the attraction and adsorption of atmospheric trace gases at the interface are the first steps of aerosol nucleation and growth. In addition, the maximum effective surface area of a cloud/fog is 0.3 $m^2$ $m^{-3}$, and this value is up to 60 $m^2$ $m^{-3}$ for snowpack.[23] Hence, such an abundance of natural aerosol surfaces suggests that the air–nanoparticle interface plays an important role in atmospheric chemistry due to its ability to align and concentrate trace gases.[24–30]

A very recent experimental study identified that higher oligomers are produced in the air–nanoparticle interfacial photochemistry of GL and hydroxyl radicals using time-of-flight secondary ion mass spectrometry.[31] Previous theoretical studies revealed that there is a catalytic effect of the interfacial water environment on the GL isomerization and hydration reaction.[32,33] However, because aerosols are moderately acidic with an average pH of 4.2,[34] sulfate and SA are considered to be important contributors to SOA formation in the nanoparticles.[35] However, up to now, no studies on the influence of nanoparticle acidity on the kinetics and thermodynamics of the role of GL in aerosol formation have been performed, hindering the accurate assessment of its roles in the formation of SOA.

Here, we investigated the atmospheric chemistry processes of GL at the air–nanoparticle interface and in the nanoparticle interior, respectively, by combining molecular dynamics (MD) simulations and quantum chemical (QC) calculations. The kinetic and thermodynamic aspects of GL at the interface of the nanoparticle, such as the free energy profiles, the molecular interactions and orientations as well as the uptake and accommodation abilities, were illustrated. The heterogeneous reaction mechanisms and kinetics of GL in the nanoparticle interior were studied and its role in the uptake of GL were assessed. The neutral and acidic systems were simulated by using neutral nanoparticles and acidic nanoparticles with the concentrations of SA between 20 wt% to 60 wt%. The impact of acidity on the uptake of GL was evaluated and the implications of our results for SOA formation were discussed.

## 2. Methods

All MD simulations were performed using the package of the NAMD program.[36] The acidic nanoparticle models with different concentrations of SA were established using the PACKMOL procedure.[37] The all dynamical configurations were visualized *via* VMD software.[38] The density of water was 1.0 g $cm^{-3}$ under ambient conditions, and the volume of the box was 2.5 × 2.5 × 2.5 $nm^3$. Moreover, according to the study of Martins-Costa *et al.*,[39] a neutral nanoparticle was simulated by including 499 water molecules in a box of 24.662 × 24.662 × 24.662 $Å^3$. Thus, the neutral nanoparticle contained 499 water molecules within a box of 2.5 × 2.5 × 2.5 $nm^3$ volume. The acidic nanoparticle was simulated by using the nanoparticle of 60 wt% SA concentration in a box of 2.6 × 2.6 × 2.6 $nm^3$ volume. The 2.5 × 2.5 × 2.5 $nm^3$ and 2.6 × 2.6 × 2.6 $nm^3$ boxes were constructed because a cluster smaller than 3.0 nm is critical for the nanoparticle to grow.[40] Acidic nanoparticles with different concentrations of SA (20 wt%, 30 wt% and 50 wt%) were also investigated (Table S1†) according to the acidity effect of nanoparticles in the troposphere.[41,42] The positions of water and SA molecules were confirmed using a MD method based on the initial positions determined by a Monte Carlo method. The 500 ps equilibration at a time step of 0.5 fs was executed in the isothermal–isochoric (*NVT*) ensemble ($T$ = 298 K) and then in the isothermal–isobaric (*NPT*) ensemble ($P$ = 1 bar) to guarantee the thermodynamic equilibrium of the neutral or acidic nanoparticle. The $Z$-axis was perpendicular to the neutral or acidic nanoparticle interface. A vacuum layer of 3.0 nm was added above the aqueous phase in order to imitate the atmospheric process of gaseous GL to the aqueous phase. The GL molecule was initially located 2.0 nm above the center of mass of the neutral or acidic nanoparticles. GL, SA and water were described by the OPLS-AA force field[43] with the restrained electrostatic potential (RESP) charge obtained by Multiwfn program,[44] CHARMM22 force field[45,46] and TIP3P force field including the implicit polarization,[39,47] respectively. The Lennard-Jones and real space coulombic interactions were cut off at 12.0 Å. The Coulomb term was determined by the Ewald summation method to an accuracy of 0.0001 kcal $mol^{-1}$. The periodic boundary conditions were used along the $X$, $Y$ and $Z$ directions. The geometric optimization of 500 steps was calculated before the MD simulation.

By using the umbrella sampling (US)[48] and the weighted-histogram analysis method (WHAM),[49] the free energy profiles along the reaction coordinate ($R$) were calculated to obtain the kinetic trajectories of GL from the gas to aqueous phase. The $R$ was defined as the distance between the center of mass of GL and that of the nanoparticle. There were 21 windows in the US simulation and the bound of the $R$ in every window was kept the same as $Z \in [0, 2.0\ \text{nm}]$. The distance was varied by steps of 0.1 nm, centered from 2.0 nm to 0 nm. The bias potential force constant was equal to 10 kcal $mol^{-1}$ $Å^{-2}$. The zero-level of the free energy profile in the WHAM analysis method was located at the free energy minimum. Additional detailed descriptions of the results are provided in the ESI.†

All QC calculations were performed by the Gaussian 09 program.[50] The polarizable continuum solvent model (SMD) suitable in the solution was used.[51] The geometric

optimization of all stationary points (SPs), including the reactants, complex, transition states (TSs) and products, was carried out using the M06-2X functional,[52] with the 6-311G(d,p) basis set,[6] *i.e.*, at the M06-2X/6-311G(d,p) level. The harmonic vibrational frequencies of SPs were calculated to ensure all SPs as either the minima (zero imaginary frequency) or a TS (exactly with only one imaginary frequency). At the same level, the thermodynamic contributions were also calculated. The intrinsic reaction coordinate theory was performed to confirm that the TS accurately connected the reactant with the corresponding product. Based on the geometric optimization, the potential energy surface (PES) was refined using the same method with a more flexible basis set 6-311+G(3df,3pd), *i.e.*, at the M06-2X/6-311+G(3df,3pd) level. All energetic parameters included thermal correction at the same level of theory. Here, the dual-level approach was denoted as the M06-2X//M06-2X level, where a single-point energy calculation at the M06-2X/6-311+G(3df,3pd) level was carried out for the geometry optimized at a lower level of M06-2X/6-311G(d,p).

The rate constants ($k$) were calculated using conventional transition state theory (TST)[53–56] as follows:

$$k = \sigma \frac{k_B T}{h} \exp\left(\frac{-\Delta G^{\ddagger}}{RT}\right) \quad (1)$$

where $k_B$ and $h$ are the Boltzmann and Planck constants, respectively; $\Delta G^{\ddagger}$ is the Gibbs free energy barrier of the reaction including the thermodynamic contribution correction; $\sigma$ represents the reaction path degeneracy, accounting for the number of equivalent reaction paths.

In addition, to simulate realistic conditions in the solution, the solvent cage effect was included according to the correction proposed by Okuno,[57] taking into account the free volume theory. The expression used to correct Gibbs free energy is as follows:

$$\Delta G_{sol}^{FV} \cong \Delta G_{sol}^{0} - RT\{\ln[n10^{(2n-2)}] - (n-1)\} \quad (2)$$

where $\Delta G_{sol}^{0}$ is the Gibbs free energy of reaction in the solution and $n$ represents the number of molecules in the reaction. According to expression (2), the cage effects in the solution cause the Gibbs free energy to decrease by 2.54 kcal mol$^{-1}$ for bimolecular reactions at 298.15 K.

Some of the calculated rate constant ($k$) values were found to be close to the diffusion-limit. Thus, the apparent rate constant ($k_{app}$) was obtained by the effect of diffusion-limit[58] besides the TST calculations:

$$k_{app} = \frac{k k_D}{k + k_D} \quad (3)$$

where the $k$ is the thermal rate constant, obtained from TST calculations from the expression (1), and $k_D$ is the steady-state rate constant for an irreversible bimolecular diffusion-controlled reaction:

$$k_D = 4\pi R D_{AB} N_A \quad (4)$$

where $R$ denotes the reaction distance, $N_A$ is Avogadro's number, and $D_{AB}$ is the mutual diffusion coefficient of the reactants A and B. $D_{AB}$ has been calculated from $D_A$ and $D_B$ according to the reference,[59] and $D_A$ and $D_B$ have been estimated from the Stokes–Einstein approach[60] listed in expression (5):

$$D = \frac{k_B T}{6\pi\eta\alpha} \quad (5)$$

where $k_B$ is the Boltzmann constant, $T$ is the temperature, $\eta$ denotes the viscosity of the solvent, which is water in our case ($\eta = 8.9 \times 10^{-4}$ Pa s), and $\alpha$ is the radius of the solute.

# 3. Results and discussion

Three essential processes are involved in the conversion of GL from the gas to aqueous phase (Fig. 1a): (1) the mutual attraction of gaseous GL and the nanoparticles (pathway I); (2) the uptake of GL at the air–nanoparticle interface (pathway II); (3) the hydration reaction of GL in the aqueous media (pathway III). Fig. 1b presents the free energy profile of the trajectories of GL traveling from air into the neutral (black line) and acidic (red line) nanoparticles.

### 3.1 The mutual attraction of gaseous GL and the nanoparticles

Fig. S1† displays the relative concentration distribution of GL and the corresponding solvent along with the direction perpendicular to the neutral or acidic nanoparticle, which is proven to be reliable to define the interfacial range.[45] Herein, according to the interfacial range, we estimate the interfacial width of air and the neutral nanoparticles (denoted as the A–N interface) and that of air and the acidic nanoparticles (indicated as the A–A interface). As described in Fig. S1,† the interfacial widths are calculated to be 8.2 Å for the A–N interface and 6.1 Å for the A–A interface, which can accommodate and uptake GL.

Here, to identify the ability of the interface to adsorb gaseous GL, the free energy difference from gaseous GL to the interface is defined as: $\Delta G_{gas\rightarrow interface} = G_{interface} - G_{gas}$, where $G_{interface}$ refers to the minimum value at the interface and $G_{gas}$ is the maximum value in the gas phase. The corresponding value reflects whether the interface prefers to adsorb gaseous GL. As depicted in Fig. 1b, the $\Delta G_{gas\rightarrow interface}$ is −3.5 kcal mol$^{-1}$ for the neutral system and −5.2 kcal mol$^{-1}$ for the acidic system, indicating that GL approaching the neutral and acidic nanoparticles is favourable thermodynamically. A higher value of $\Delta G_{gas\rightarrow interface}$ for the acidic system suggests that the acidic nanoparticle interface displays a preference for the uptake of gaseous GL.

### 3.2 The uptake of GL at the air–nanoparticle interface

The typical snapshots from the trajectories of pathway I to pathway II are displayed in Fig. 2. Herein, the configurations A and A′ (Con A and Con A′) point to the

 

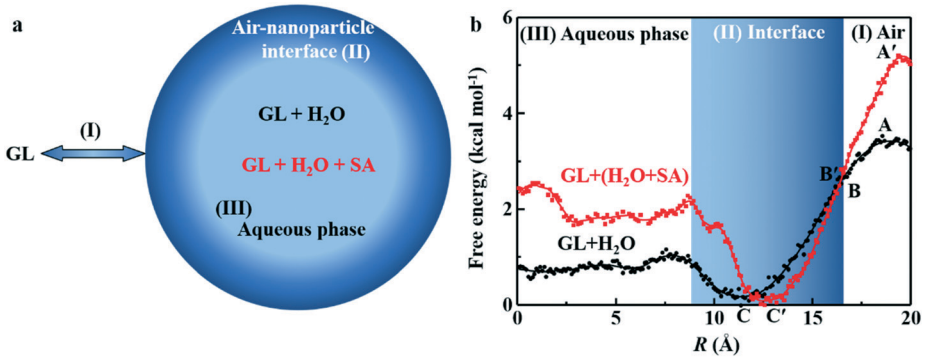


**Fig. 1** (a) Three essential processes of gaseous GL reaction with the nanoparticles. (b) The free energy profile of gaseous GL approaching the neutral (black line) and acidic (red line) nanoparticles. The width of interface is the sum of the A–N and A–A interfaces.

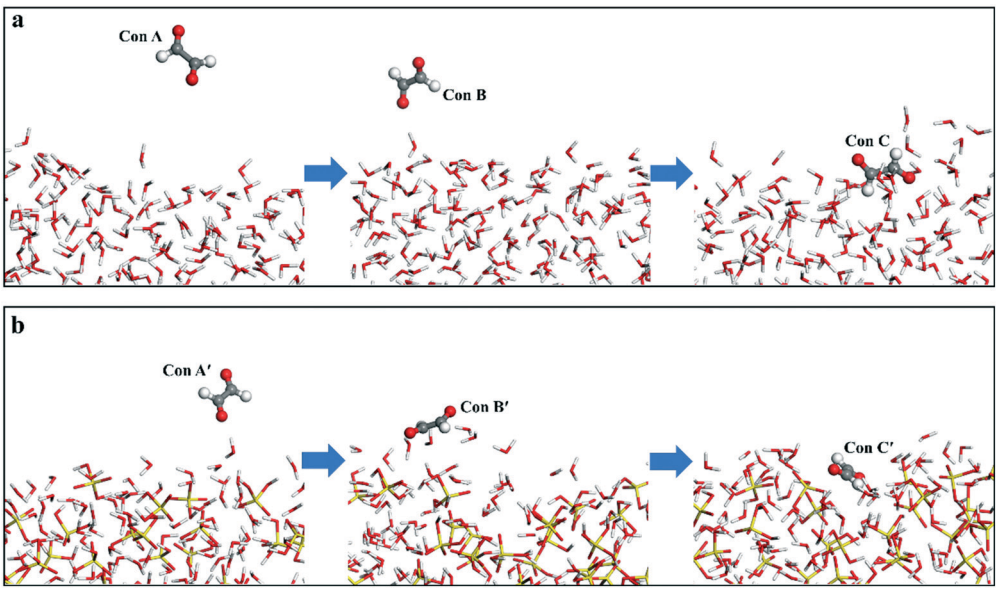


**Fig. 2** Typical snapshots from the trajectories of pathway I to pathway II in (a) the neutral and (b) acidic systems, respectively. The Con A and Con A′ point to the structures located at the free energy maximum in the neutral (point A in Fig. 1b) and acidic (point A′ in Fig. 1b) systems, respectively. The Con B and Con B′ are the snapshots on the A–N (point B in Fig. 1b) and A–A (point B′ in Fig. 1b) surfaces, which are the bounds between the gas phase and the corresponding interface, respectively. The Con C and Con C′ represent the free energy minimum at the neutral (point C in Fig. 1b) and acidic (point C′ in Fig. 1b) nanoparticle interfaces, respectively.

structures located at the free energy maximum in the neutral (point A in Fig. 1b) and acidic (point A′ in Fig. 1b) systems, respectively. The configurations B and B′ (Con B and Con B′) correspond to the snapshots on the A–N (point B in Fig. 1b) and A–A (point B′ in Fig. 1b) surfaces, which are the bounds between the gas phase and the corresponding interface, respectively. The configurations C and C′ (Con C and Con C′) represent the free energy minimum at the neutral (point C in Fig. 1b) and acidic (point C′ in Fig. 1b) nanoparticle interfaces, respectively. The configurations presented in Fig. 2a and b represent the total energy minimum at the corresponding window, *i.e.*, the most stable configuration at the corresponding window. In these configurations, a preferential orientation of the C═O group in GL is directly towards the interface rather than parallel to the interface. In addition, to further confirm the orientation of GL with respect to the interface, 100 typical snapshots around the free energy minimum at the interface are chosen to estimate the angular distribution of GL (Fig. 3). These typical snapshots are the 100 configurations with the lowest total energy among all the configurations at the window of the free energy minimum. Here, the angular distribution is depicted using the $\theta$ value, which is the angle formed between the $Z$-axis (perpendicular to the interface) and the C═O bond. As shown in Fig. 3, the $\theta$ values are mainly located in the 40–90° range in the neutral system, implying that the carbonyl O-atom prefers to point to the interface. Similarly, in the acidic system, the angled orientation of GL to the interface changes from almost vertical to nearly parallel (Con A′ → Con B′ → Con C′) along the reaction trajectories (Fig. 2b), and the $\theta$ values vary in the range of 40–90°. As discussed above, all evidence

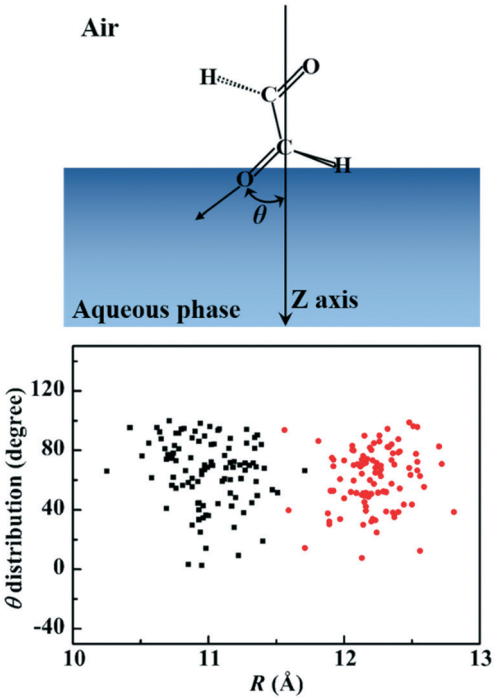


Fig. 3 Angular distribution of GL with respect to the A–N (black square) and A–A (red circle) interfaces. The *Z*-axis is defined as the axis perpendicular to the interface and the $\theta$ is the angle formed between the *Z*-axis and the C=O bond of GL.

indicates that the C=O group of GL exhibits a preferential orientation to both the A–N and A–A interfaces.

The solvation effect at the interface region depends on the role of the orientations of the solute because different orientations correspond to different interactions between the solute and nanoparticles.[24] The hydrogen bonding (HB) is a key factor in determining the average orientation of the solute with respect to the interface. In this work, the two types of HBs at the interface are studied: the H atom of GL and O atom of water ($H_{GL}$–$O_{water}$), and the O atom of GL and H atom of water ($O_{GL}$–$H_{water}$). The ranges of bond length and angle in a HB (H···O) interaction are from 1.496 Å to 2.383 Å, and 123.7° to 178.1°, respectively.[61] The radial distribution function ($g(r)$) is usually used to describe how the density of surrounding matter varies as a function of the distance from a point and can be used to depict the close interaction of two specific atoms. In order to describe the HB formation, the $g(r)$s of two types of HBs between GL and the interface in the neutral and acidic systems are estimated and illustrated in Fig. 4. As displayed in Fig. 4a, no apparent peak of $H_{GL}$–$O_{water}$ within 2.5 Å suggests that the stability of GL at the interface is not impacted by the interaction between $H_{GL}$ and $O_{water}$ atoms in the neutral and acidic systems. As delineated in Fig. 4b, the intensity of the peak for the acidic system is stronger in comparison of that for the neutral system, indicating that the probability of $O_{GL}$–$H_{water}$ is enhanced in the presence of SA.

The coordination number ($N$) is estimated *via* the integration of the $g(r) \times r^2$ function up to $r$ = 2.5 Å (first minimum). This parameter can reflect the number of water molecules associated with GL in the solvation shell (Fig. 5 and Table S2†). A decrease between the neutral ($N$ = 2.9) and the acidic ($N$ = 2.2) systems is explained in that the number of $H_{water}$ atoms exposed at the neutral nanoparticle interface is larger than that at the acidic nanoparticle interface. Hereby, in our work, the excess stability of GL at the A–A interface is not due to growing GL–water interactions but probably due to the modification of SA–water solvation terms. This result further suggests that SA makes the acidic nanoparticle interface the perfect region to adsorb and accommodate GL. The configurations, the free energies, and the trajectories during the approach of gaseous GL to acidic nanoparticles with different concentrations of SA (20 wt%, 30 wt% and 50 wt%) were also investigated, and the results are listed in Fig. S2 and S3.† Similar results can be drawn from the other acidic systems. That is, the acidic nanoparticle interface exhibits a better ability to adsorb gaseous GL and accommodate GL relative to the neutral nanoparticle interface.

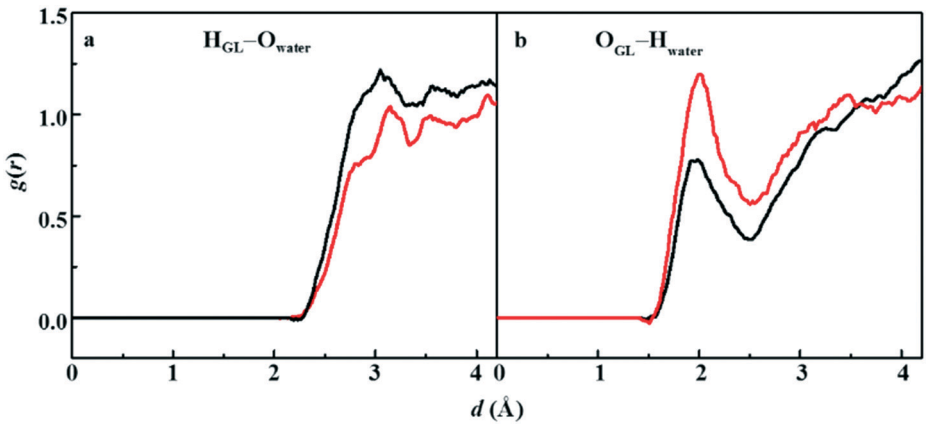


Fig. 4 Radial distribution functions ($g(r)$s) of the (a) $H_{GL}$–$O_{water}$ and (b) $O_{GL}$–$H_{water}$ hydrogen bonds for the interface in the neutral (black line) and acidic (red line) systems.

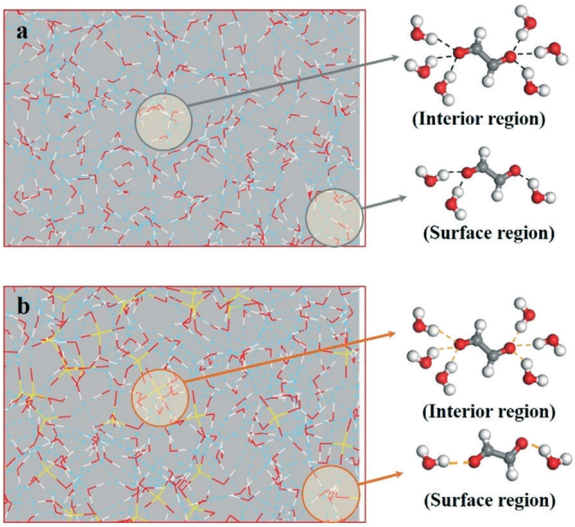


Fig. 5 Coordination number ($N$) of water molecules combined with GL at the interface and in the nanoparticle interior region for (a) the neutral and (b) acidic systems.

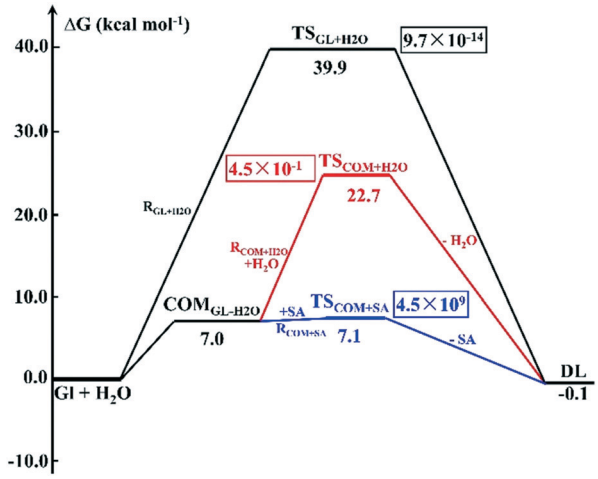


Fig. 6 The potential energy surface of the hydration reaction of GL in the neutral and acidic systems. The black line represents the direct hydration reaction of GL ($R_{GL+H_2O}$). The red and blue lines represent the indirect hydration reaction of $COM_{GL-H_2O}$ with $H_2O$ and SA ($R_{COM+H_2O}$ and $R_{COM+SA}$), respectively. The unit of the rate constant is $M^{-1}$ $s^{-1}$.

### 3.3 The hydration reaction of GL in the aqueous media

From Fig. 1b, the stabilized GL that adsorbed to the interface subsequently enters the nanoparticle interior region (pathway III). The above process proceeds endothermically and the endothermic energy (2.3 kcal $mol^{-1}$) in the acidic system is larger than that (1.1 kcal $mol^{-1}$) in the neutral system (Fig. 1b). Furthermore, we also assessed the $N$ parameters in the aqueous phase (Fig. 5b and Table S2†). The values of 6.0 and 6.3 in the neutral and acidic systems, respectively, are both larger than those at the corresponding interfaces. It implies that GL prefers to undergo the subsequent hydration reaction in the acidic system.

In the aqueous media, GL engages in the association reaction with water to form a diol (DL).[17,62] The PES of the direct hydration reaction of GL and water ($R_{GL+H_2O}$ in Fig. 6) was calculated. The $\Delta G^{\ddagger}$ and reaction energy ($\Delta G_r$) are 39.9 kcal $mol^{-1}$ and −0.1 kcal $mol^{-1}$, respectively. The corresponding rate constant ($k_{GL+H_2O}$) is $9.7 \times 10^{-14}$ $M^{-1}$ $s^{-1}$. It suggests that the direct hydration reaction of GL is dynamically and thermodynamically unfeasible.

According to a recent study, GL readily associates with $H_2O$ to form a complex ($COM_{GL-H_2O}$), which subsequently reacts with $H_2O$ or SA.[20] Hence, there exists two indirect hydration reaction pathways, as shown in Fig. 6: $R_{COM+H_2O}$, $COM_{GL-H_2O}$ reaction with $H_2O$ and $R_{COM+SA}$, $COM_{GL-H_2O}$ with SA. The $R_{COM+H_2O}$ corresponds to a large $\Delta G^{\ddagger}$ of 22.7 kcal $mol^{-1}$ and a slight $\Delta G_r$ of −0.1 kcal $mol^{-1}$. Although the rate constant increases 13 orders of magnitude to be $4.5 \times 10^{-1}$ $M^{-1}$ $s^{-1}$, the hydration reaction of GL involving an extra water molecule to form DL ($R_{COM+H_2O}$) is of minor importance in the neutral nanoparticle. As shown in Fig. 6, the $\Delta G^{\ddagger}$ of $R_{COM+SA}$ is 7.1 kcal $mol^{-1}$, which is 15.6 kcal $mol^{-1}$ and 32.8 kcal $mol^{-1}$ lower than those of $R_{COM+H_2O}$ and $R_{GL+H_2O}$. The corresponding rate constant of $R_{COM+SA}$ of $4.5 \times 10^{9}$ $M^{-1}$ $s^{-1}$ is larger by 10 and 23 orders of magnitude than that of $R_{COM+H_2O}$ and $R_{GL+H_2O}$, respectively. In addition, previous studies have also revealed that the complexation of GL hydrates with sulfate can enhance the uptake of GL.[63,64] Hence, SA and sulfate can accelerate the hydration reaction of GL in the interior region of the nanoparticle. This is in line with the experimental results that acid can catalyze the heterogeneous reaction of GL in the aqueous phase.[13,18] The result implies that the enhanced consumption of GL in the acidic aqueous media indirectly promotes the continuous uptake and accommodation of GL at the acidic nanoparticle interface.

The vibrational frequencies, thermal corrections, absolute energies, and Cartesian coordinates of the relevant species involved in the direct and indirect hydration reactions mentioned above are included in Table S3.† Our calculated $\Delta G^{\ddagger}$ value of $R_{GL+H_2O}$ is nearly double that from a previous theoretical study (18.5 kcal $mol^{-1}$),[62] which obtained the solvent energies based on the optimized gas-phase geometry, in contrast to our present approach using the optimized aqueous-phase geometry (Methods). The $\Delta G^{\ddagger}$ of $R_{COM+H_2O}$ from a very recent theoretical study is 14.5 kcal $mol^{-1}$,[10] which obtained the barrier energy based on the quadratic synchronous transit approach (QST2) geometry by using PCM solvation. It is somewhat lower than our calculated value, which is obtained by using SMD solvation based on opt = TS geometry. To further evaluate the results at the M06-2X//M06-2X level, a higher level calculation using the CCSD(T)/6-311+G(2df,2p) level was performed to refine the energetics for the reaction pathway of $R_{GL+H_2O}$. The $\Delta G^{\ddagger}$ value of 39.9 kcal $mol^{-1}$ for $TS_{GL+H_2O}$ at the M06-2X//M06-2X level is only slightly lower than that at the CCSD(T)/6-311+G(2df,2p)//M06-2X/6-311G(d,p) level (44.1 kcal $mol^{-1}$). The error in the $\Delta G_r$ value between the two methods is within 1% for the reaction pathway of $R_{GL+H_2O}$, indicating that the M06-2X//M06-2X level provides reliable data.

## 4. Conclusions and atmospheric implications

Small α-dicarbonyls exist in high abundance in urban environments because of their large yields from the photochemical oxidation of aromatics[5,6] that are emitted in large amounts from traffic and industrial sources.[65] In the gas-phase, photolysis or reaction with hydroxyl radicals has been identified as the major loss process for GL, with an estimated lifetime of several hours to about one day for typical tropospheric conditions.[66,67] Alternatively, GL is involved in particle-phase reactions or cloud-processing, which contributes to atmospheric SOA formation.[16–18] The previous experimental and theoretical studies mainly focus on the oligomerization reaction of GL and its contribution to SOA formation.[10,15,16,62] A very recent experimental study has pointed out that the interfacial process plays an important role in the SOA formation through the reaction of GL and hydroxyl radicals.[31] Hence, we investigated the uptake of GL at the A–N and A–A interface using MD simulations and the subsequent hydration reaction of GL in the neutral and acidic nanoparticles by means of QC calculations. Our MD simulation results reveal that the acidic nanoparticle interface exhibits a better ability to adsorb gaseous GL and accommodate GL relative to the neutral nanoparticle interface.

The acidity of the aerosol is in the range of the SA concentration of 1–60 wt% in the lower troposphere,[41,42] and the hydronium ion has a stronger surface tendency than the bisulfate and sulfate ions.[68] Our MD results indicate that the C═O group of GL shows a preferential orientation to the acidic nanoparticle interface. Moreover, we investigated the natural bond orbital (NBO) of GL. The carbonyl O-atom exhibits a negative charge of −0.532*e*. This implies that the electrostatic attraction facilitates the uptake of GL to the acidic nanoparticle interface. Subsequently, our QC results show that SA can accelerate the hydration reaction of GL in the interior region of the nanoparticle. Kurtén *et al.* also confirmed that the complexation of GL hydrates with sulfate can increase the uptake of GL.[63] The hydration reaction of GL is considered the first step of the oligomerization for GL, leading to oligomeric products which contribute to SOA growth.[15,17] Our MD and QC results clarify the enhanced uptake of GL at the acidic nanoparticle interface, highlighting the necessity to account for the interfacial process when assessing SOA formation. Hence, future experimental and theoretical studies need to focus on the oligomerization reactions of small α-dicarbonyls at the acidic nanoparticle interface.

## Conflicts of interest

There are no conflicts to declare.

## Acknowledgements

This work was financially supported by National Natural Science Foundation of China (41675122, 41731279 and 41907184), Natural Science Foundation of Guangdong Province, China (2019B151502064), Science and Technology Program of Guangzhou City (201707010188), National Natural Science Funds for Distinguished Young Scholars (41425015), Local Innovative and Research Teams Project of Guangdong Pearl River Talents Program (2017BT01Z032), Innovation Team Project of Guangdong Provincial Department of Education (2017KCXTD012), Science and Technology Key Project of Guangdong Province, China (2019B110206002) and the China Postdoctoral Science Foundation Grant (2018M633016).

## Notes and references

1 R. Zhang, G. Wang, S. Guo, M. L. Zamora, Q. Ying, Y. Lin, W. Wang, M. Hu and Y. Wang, Formation of urban fine particulate matter, *Chem. Rev.*, 2015, **115**, 3803–3855.
2 Z. An, R. J. Huang, R. Zhang, X. Tie, G. Li, J. Cao, W. Zhou, Z. Shi, Y. Han, Z. Gu and Y. Ji, Severe haze in northern China: A synergy of anthropogenic emissions and atmospheric processes, *Proc. Natl. Acad. Sci. U. S. A.*, 2019, **116**, 8657–8666.
3 R. J. Huang, Y. Zhang, C. Bozzetti, K. F. Ho, J. J. Cao, Y. Han, K. R. Daellenbach, J. G. Slowik, S. M. Platt, F. Canonaco, P. Zotter, R. Wolf, S. M. Pieber, E. A. Bruns, M. Crippa, G. Ciarelli, A. Piazzalunga, M. Schwikowski, G. Abbaszade, J. Schnelle-Kreis, R. Zimmermann, Z. An, S. Szidat, U. Baltensperger, I. El Haddad and A. S. Prevot, High secondary aerosol contribution to particulate pollution during haze events in China, *Nature*, 2014, **514**, 218–222.
4 K. Mitsuishi, M. Iwasaki, M. Takeuchi, H. Okochi, S. Kato, S.-I. Ohira and K. Toda, Diurnal variations in partitioning of stmospheric glyoxal and methylglyoxal between gas and particles at the ground level and in the free troposphere, *ACS Earth Space Chem.*, 2018, **2**, 915–924.
5 R. Volkamer, U. Platt and K. Wirtz, Primary and secondary glyoxal formation from aromatics: experimental evidence for the bicycloalkyl–radical pathway from benzene, toluene, and p-xylene, *J. Phys. Chem. A*, 2001, **105**, 7865–7874.
6 Y. Ji, J. Zhao, H. Terazono, K. Misawa, N. P. Levitt, Y. Li, Y. Lin, J. Peng, Y. Wang, L. Duan, B. Pan, F. Zhang, X. Feng, T. An, W. Marrero-Ortiz, J. Secrest, A. L. Zhang, K. Shibuya, M. J. Molina and R. Zhang, Reassessing the atmospheric oxidation mechanism of toluene, *Proc. Natl. Acad. Sci. U. S. A.*, 2017, **114**, 8169–8174.
7 H. J. Lim, A. G. Carlton and B. J. Turpin, Isoprene forms secondary organic aerosol through cloud processing: model simulations, *Environ. Sci. Technol.*, 2005, **39**, 4441–4446.
8 T. M. Fu, D. J. Jacob, F. Wittrock, J. P. Burrows, M. Vrekoussis and D. K. Henze, Global budgets of atmospheric glyoxal and methylglyoxal, and implications for formation of secondary organic aerosols, *J. Geophys. Res.: Atmos.*, 2008, **113**, D15303–D15319.
9 W. Marrero-Ortiz, M. Hu, Z. Du, Y. Ji, Y. Wang, S. Guo, Y. Lin, M. Gomez-Hermandez, J. Peng, Y. Li, J. Secrest, M. L. Zamora, Y. Wang, T. An and R. Zhang, Formation and

 

Optical Properties of Brown Carbon from Small alpha-Dicarbonyls and Amines, *Environ. Sci. Technol.*, 2019, **53**, 117–126.

10 V. P. Tuguldurova, A. V. Fateev, O. K. Poleshchuk and O. V. Vodyankina, Theoretical analysis of glyoxal condensation with ammonia in aqueous solution, *Phys. Chem. Chem. Phys.*, 2019, **21**, 9326–9334.

11 M. H. Powelson, B. M. Espelien, L. N. Hawkins, M. M. Galloway and D. O. De Haan, Brown carbon formation by aqueous-phase carbonyl compound reactions with amines and ammonium sulfate, *Environ. Sci. Technol.*, 2014, **48**, 985–993.

12 A. K. Lee, R. Zhao, R. Li, J. Liggio, S. M. Li and J. P. Abbatt, Formation of light absorbing organo-nitrogen species from evaporation of droplets containing glyoxal and ammonium sulfate, *Environ. Sci. Technol.*, 2013, **47**, 12819–12826.

13 M. Jang, N. M. Czoschke, S. Lee and R. M. Kamens, Heterogeneous atmospheric aerosol production by acid-catalyzed particle-phase reactions, *Science*, 2002, **298**, 814–817.

14 Y. B. Lim, Y. Tan, M. J. Perri, S. P. Seitzinger and B. J. Turpin, Aqueous chemistry and its role in secondary organic aerosol (SOA) formation, *Atmos. Chem. Phys.*, 2010, **10**, 10521–10539.

15 M. E. Gomez, Y. Lin, S. Guo and R. Zhang, Heterogeneous chemistry of glyoxal on acidic solutions. An oligomerization pathway for secondary organic aerosol formation, *J. Phys. Chem. A*, 2015, **119**, 4457–4463.

16 J. Liggio, S. M. Li and R. Mclaren, Heterogeneous reactions of glyoxal on particulate matter: identification of acetals and sulfate esters, *Environ. Sci. Technol.*, 2005, **39**, 1532–1541.

17 K. W. Loeffler, C. A. Koehler, N. M. Paul and D. O. De Haan, Oligomer formation in evaporating aqueous glyoxal and methyl glyoxal solutions, *Environ. Sci. Technol.*, 2006, **40**, 6318–6323.

18 J. Liggio, S. M. Li and R. McLaren, Reactive uptake of glyoxal by particulate matter, *J. Geophys. Res.: Atmos.*, 2005, **110**, D10304–D10316.

19 M. Jang and R. M. Kamens, Atmospheric secondary aerosol formation by heterogeneous reactions of aldehydes in the presence of a sulfuric acid aerosol catalyst, *Environ. Sci. Technol.*, 2001, **35**, 4758–4766.

20 M. Q. Huang, S. Y. Cai, Y. M. Liao, W. X. Zhao, C. J. Hu, Z. Y. Wang and W. J. Zhang, Theoretical studies on mechanism and rate constant of gas phase hydrolysis of glyoxal catalyzed by sulfuric acid, *Chin. J. Chem. Phys.*, 2016, **29**, 335–343.

21 J. Zhong, M. Kumar, J. M. Anglada, M. T. C. Martins-Costa, M. F. Ruiz-Lopez, X. C. Zeng and J. S. Francisco, Atmospheric spectroscopy and photochemistry at environmental water interfaces, *Annu. Rev. Phys. Chem.*, 2019, **70**, 45–69.

22 J. Zhong, M. Kumar, J. S. Francisco and X. C. Zeng, Insight into Chemistry on Cloud/Aerosol Water Surfaces, *Acc. Chem. Res.*, 2018, **51**, 1229–1237.

23 C. George, M. Ammann, B. D'Anna, D. J. Donaldson and S. A. Nizkorodov, Heterogeneous photochemistry in the atmosphere, *Chem. Rev.*, 2015, **115**, 4218–4258.

24 M. T. Martins-Costa, F. F. Garcia-Prieto and M. F. Ruiz-Lopez, Reactivity of aldehydes at the air-water interface. Insights from molecular dynamics simulations and ab initio calculations, *Org. Biomol. Chem.*, 2015, **13**, 1673–1679.

25 P. Jungwirth and D. J. Tobias, Chloride anion on aqueous clusters, at the air–water interface, and in liquid water: solvent effects on Cl- polarizability, *J. Phys. Chem. A*, 2002, **106**, 379–383.

26 S. Gopalakrishnan, P. Jungwirth, D. J. Tobias and H. C. Allen, Air-liquid interfaces of aqueous solutions containing ammonium and sulfate: spectroscopic and molecular dynamics studies, *J. Phys. Chem. B*, 2005, **109**, 8861–8872.

27 J. Zhong, C. Zhu, L. Li, G. L. Richmond, J. S. Francisco and X. C. Zeng, Interaction of SO2 with the Surface of a Water Nanodroplet, *J. Am. Chem. Soc.*, 2017, **139**, 17168–17174.

28 M. T. C. Martins-Costa, J. M. Anglada, J. S. Francisco and M. F. Ruiz-Lopez, Photochemistry of SO2 at the air-water interface: a source of OH and HOSO radicals, *J. Am. Chem. Soc.*, 2018, **140**, 12341–12344.

29 C. F. Fu and S. X. Tian, Thermodynamics of ammonia and ammonium ion at the aqueous solution–air interfaces, *J. Phys. Chem. C*, 2013, **117**, 13011–13020.

30 J. Zhong, H. Li, M. Kumar, J. Liu, L. Liu, X. Zhang, X. C. Zeng and J. S. Francisco, Mechanistic insight into the reaction of organic acids with SO3 at the air-water interface, *Angew. Chem., Int. Ed.*, 2019, **58**, 8351–8355.

31 F. Zhang, X. Yu, X. Sui, J. Chen, Z. Zhu and X. Y. Yu, Evolution of aqSOA from the air-liquid interfacial photochemistry of glyoxal and hydroxyl radicals, *Environ. Sci. Technol.*, 2019, **53**, 10236–10245.

32 C. Zhu, S. Kais, X. C. Zeng, J. S. Francisco and I. Gladich, Interfaces select specific stereochemical conformations: the isomerization of glyoxal at the liquid water interface, *J. Am. Chem. Soc.*, 2017, **139**, 27–30.

33 Y. Wang, Y. Tang and Y. Shao, Catalytic influence of water and formic acid molecules on hydration of methylglyoxal in atmosphere, *Comput. Theor. Chem.*, 2017, **1112**, 71–81.

34 M. Liu, Y. Song, T. Zhou, Z. Xu, C. Yan, M. Zheng, Z. Wu, M. Hu, Y. Wu and T. Zhu, Fine particle pH during severe haze episodes in northern China, *Geophys. Res. Lett.*, 2017, **44**, 5213–5221.

35 M. Sipilä, T. Berndt, T. Petäjä, D. Brus, J. Vanhanen, F. Stratmann, J. Patokoski, R. L. Mauldin III, A. P. Hyvärinen, H. Lihavainen and M. Kulmala, The role of sulfuric acid in atmospheric nucleation, *Science*, 2010, **327**, 1243–1247.

36 J. C. Phillips, R. Braun, W. Wang, J. Gumbart, E. Tajkhorshid, E. Villa, C. Chipot, R. D. Skeel, L. Kale and K. Schulten, Scalable molecular dynamics with NAMD, *J. Comput. Chem.*, 2005, **26**, 1781–1802.

37 L. Martínez, R. Andrade, E. G. Birgin and J. M. Martínez, Software news and update packmol: a package for building initial configurations for molecular dynamics simulations, *J. Comput. Chem.*, 2009, **30**, 2157–2164.

38 W. Humphrey, A. Dalke and K. Schulten, VMD: Visual molecular dynamics, *J. Mol. Graphics*, 1996, **14**, 33–38.
39 M. T. Martins-Costa, J. M. Anglada, J. S. Francisco and M. F. Ruiz-Lopez, Reactivity of volatile organic compounds at the surface of a water droplet, *J. Am. Chem. Soc.*, 2012, **134**, 11821–11827.
40 L. Yao, O. Garmash, F. Bianchi, J. Zheng, C. Yan, J. Kontkanen, H. Junninen, S. B. Mazon, M. Ehn, P. Paasonen, M. Sipilä, M. Wang, X. Wang, S. Xiao, H. Chen, Y. Lu, B. Zhang, D. Wang, Q. Fu, F. Geng, L. Li, H. Wang, L. Qiao, X. Yang, J. Chen, V. M. Kerminen, T. Petäjä, D. R. Worsnop, M. Kulmala and L. Wang, Atmospheric new particle formation from sulfuric acid and amines in a Chinese megacity, *Science*, 2018, **361**, 278–281.
41 J. Curtius, B. Sierau, F. Arnold, M. de Reus, J. Ström, H. A. Scheeren and J. Lelieveld, Measurement of aerosol sulfuric acid: 2. Pronounced layering in the free troposphere during the second Aerosol Characterization Experiment (ACE 2), *J. Geophys. Res.: Atmos.*, 2001, **106**, 31975–31990.
42 R. L. Tanner, B. P. Leaderer and J. D. Spengler, Acidity of atmospheric aerosols, *Environ. Sci. Technol.*, 1981, **15**, 1150–1153.
43 W. L. Jorgensen, D. S. Maxwell and J. Tirado-Rives, Development and testing of the OPLS all-atom force field on conformational energetics and properties of organic liquids, *J. Am. Chem. Soc.*, 1996, **118**, 11225–11236.
44 L. Tian and C. Feiwu, Multiwfn: a multifunctional wavefunction analyzer, *J. Comput. Chem.*, 2012, **33**, 580–592.
45 W. Zhang, Y. Ji, G. Li, Q. Shi and T. An, The heterogeneous reaction of dimethylamine/ammonia with sulfuric acid to promote the growth of atmospheric nanoparticles, *Environ. Sci.: Nano*, 2019, **6**, 2767–2776.
46 V. Zoete, M. A. Cuendet, A. Grosdidier and O. Michielin, SwissParam: a fast force field generation tool for small organic molecules, *J. Comput. Chem.*, 2011, **32**, 2359–2368.
47 P. Mark and L. Nilsson, Structure and dynamics of the TIP3P, SPC, and SPC/E water models at 298 K, *J. Phys. Chem. A*, 2001, **105**, 9954–9960.
48 G. M. Torrie and J. P. Valleau, Nonphysical sampling distributions in Monte Carlo free-energy estimation: Umbrella sampling, *J. Comput. Phys.*, 1977, **23**, 187–199.
49 S. Kumar, D. Bouzida, R. H. Swendsen, P. A. Kollman and J. M. Rosenberg, The weighted histogram analysis method for free-energy calculations on biomolecules. i. the method, *J. Comput. Chem.*, 1992, **13**, 1011–1021.
50 M. J. Frisch, G. W. Trucks, H. B. Schlegel, G. E. Scuseria, M. A. Robb, J. R. Cheeseman, G. Scalmani, V. Barone, B. Mennucci, G. A. Petersson, H. Nakatsuji, M. Caricato, X. Li, H. P. Hratchian, A. F. Izmaylov, J. Bloino, G. Zheng, J. L. Sonnenberg, M. Hada, M. Ehara, K. Toyota, R. Fukuda, J. Hasegawa, M. Ishida, T. Nakajima, Y. Honda, O. Kitao, H. Nakai, T. Vreven, J. A. Montgomery, Jr., J. E. Peralta, F. Ogliaro, M. Bearpark, J. J. Heyd, E. Brothers, K. N. Kudin, V. N. Staroverov, T. Keith, R. Kobayashi, J. Normand, K. Raghavachari, A. Rendell, J. C. Burant, S. S. Iyengar, J. Tomasi, M. Cossi, N. Rega, J. M. Millam, M. Klene, J. E. Knox, J. B. Cross, V. Bakken, C. Adamo, J. Jaramillo, R. Gomperts, R. E. Stratmann, O. Yazyev, A. J. Austin, R. Cammi, C. Pomelli, J. W. Ochterski, R. L. Martin, K. Morokuma, V. G. Zakrzewski, G. A. Voth, P. Salvador, J. J. Dannenberg, S. Dapprich, A. D. Daniels, O. Farkas, J. B. Foresman, J. V. Ortiz, J. Cioslowski and D. J. Fox, *Gaussian 09, Revision D.01*, Gaussian, Inc., Wallingford CT, 2013.
51 A. V. Marenich, C. J. Cramer and D. G. Truhlar, Universal solvation model based on solute electron density and on a continuum model of the solvent defined by the bulk dielectric constant and atomic surface tensions, *J. Phys. Chem. B*, 2009, **113**, 6378–6396.
52 Y. Zhao and D. G. Truhlar, The M06 suite of density functionals for main group thermochemistry, thermochemical kinetics, noncovalent interactions, excited states, and transition elements: two new functionals and systematic testing of four M06-class functionals and 12 other functionals, *Theor. Chem. Acc.*, 2008, **120**, 215–241.
53 Y. Gao, Y. Ji, G. Li and T. An, Mechanism, kinetics and toxicity assessment of OH-initiated transformation of triclosan in aquatic environments, *Water Res.*, 2014, **49**, 360–370.
54 H. Eyring, The activated complex in chemical reactions, *J. Chem. Phys.*, 1935, **3**, 107–115.
55 M. G. Evans and M. G. Polanyi, Some applications of the transition state method to the calculation of reaction velocities,especially in solution, *Trans. Faraday Soc.*, 1935, **31**, 875–894.
56 A. Galano, J. R. Alvarez-Idaboy, G. Annia and A. I. J. Raul, Guanosine + OH radical reaction in aqueous solution: a reinterpretation of the UV-vis data based on thermodynamic and kinetic calculations, *Org. Lett.*, 2009, **11**, 5114–5117.
57 Y. Okuno, Theoretical investigation of the mechanism of the baeyer-villiger reaction in nonpolar solvents, *Chem. – Eur. J.*, 1997, **3**, 210–218.
58 F. C. Collins and G. E. Kimball, Diffusion-controlled reaction rates, *J. Colloid Sci.*, 1949, **4**, 425–437.
59 D. G. Truhlar, Nearly encounter-controlled reactions: The equivalence of the steady-state and diffusional viewpoints, *J. Chem. Educ.*, 1985, **62**, 104–106.
60 A. Einstein, Über die von der molekularkinetischen Theorie der Wärme geforderte Bewegung von in ruhenden Flüssigkeiten suspendierten Teilchen, *Ann. Phys.*, 1905, **322**, 549–560.
61 J. Zhao, A. Khalizov, R. Zhang and R. McGraw, Hydrogen-bonding interaction in molecular complexes and clusters of aerosol nucleation precursors, *J. Phys. Chem. A*, 2009, **113**, 680–689.
62 J. Kua, S. W. Hanley and D. O. Haan, Thermodynamics and kinetics of glyoxal dimer formation: a computational study, *J. Phys. Chem. A*, 2008, **112**, 66–72.
63 T. Kurtén, J. Elm, N. L. Prisle, K. V. Mikkelsen, C. J. Kampf, E. M. Waxman and R. Volkamer, Computational study of the effect of glyoxal-sulfate clustering on the Henry's law coefficient of glyoxal, *J. Phys. Chem. A*, 2015, **119**, 4509–4514.

 

64 C. J. Kampf, E. M. Waxman, J. G. Slowik, J. Dommen, L. Pfaffenberger, A. P. Praplan, A. S. Prévôt, U. Baltensperger, T. Hoffmann and R. Volkamer, Effective Henry's law partitioning and the salting constant of glyoxal in aerosols containing sulfate, *Environ. Sci. Technol.*, 2013, **47**, 4236–4244.

65 A. J. Kean, E. Grosjean, D. Grosjean and R. A. Harley, On-road measurement of carbonyls in California light-duty vehicle emissions, *Environ. Sci. Technol.*, 2001, **35**, 4198–4204.

66 J. Tadić, G. K. Moortgat and K. Wirtz, Photolysis of glyoxal in air, *J. Photochem. Photobiol., A*, 2006, **177**, 116–124.

67 B. Long, X. F. Tan, D. S. Ren and W. J. Zhang, Theoretical study on the water-catalyzed reaction of glyoxal with OH radical, *J. Mol. Struct.: THEOCHEM*, 2010, **956**, 44–49.

68 W. Hua, D. Verreault and H. C. Allen, Relative order of sulfuric acid, bisulfate, hydronium, and cations at the air-water interface, *J. Am. Chem. Soc.*, 2015, **137**, 13920–13926.